AIAA JOURNAL
Vol. 48, No. 5, May 2010

Stochastic Investigation of Flows About Airfoils at Transonic Speeds

J.-C. Chassaing*
Université Pierre et Marie Curie, 75005 Paris, France
and
D. Lucor†
Centre National de la Recherche Scientifique, 75005 Paris, France

DOI: 10.2514/1.42637

In this study, a deterministic compressible solver is coupled to a nonintrusive stochastic spectral projection method to propagate several aerodynamic uncertainties through a transonic steady flow around a NACA0012 airfoil. The stochastic model is solved in a generalized polynomial chaos framework. This approach combines the advantage of not modifying the existing deterministic solver while maintaining accurate representations of the stochastic solution and its statistics. The major difficulty of this work is to deal with deterministic transonic flows for which aerodynamics nonlinearities are reported in the uncertain probabilistic space. The efficiency of the present methodology are evaluated for the propagation of random disturbances associated with the angle of attack and the freestream Mach number. An error analysis is carried out in order to determine appropriate physical and stochastic discretization levels. Different stochastic flow regimes are analyzed in details by means of various postprocessing procedures, including error bars, probabilistic density function of the aerodynamic field, and Sobol's coefficients.

I. Introduction

THE development of design methodologies with minimum sensitivity to inherent fluctuations of the operating conditions or to the manufacturing process is of crucial importance in aerospace engineering. Nonlinear aerodynamic or aeroelastic systems subject to random parameters can result in poor offdesign performances or may exhibit losses of dynamic stability due to the presence of stochastic limit cycle oscillations (LCOs). Uncertainty quantification plays an important role in reliability assessment. It is essentially a study of variabilities, their reduction, their description, and their consequences. Such analysis can be viewed as the determination of error bars to be assigned to the numerical solution algorithms, and its application is of great importance in reliability assessment. Classical Monte Carlo or quasi-Monte Carlo simulations can provide statistical moments and probability density functions of some outputs of interest such as the pitch amplitude response of LCO. However, such approaches become impractical when each sample realization results from high-fidelity computational fluid and structural dynamics tools. Probabilistic collocation methodologies are promising candidates to get more insights into physical mechanisms of flutter and LCO [1,2] with affordable computational cost [3–5]. These studies are generally based on the use of ad hoc inviscid linear aerodynamics, and the stochastic response of the system is governed by the uncertainties associated with the nonlinear structural stiffness coefficients [5,6].

Another challenging and complementary task is the development of a numerical method for stochastic fluid–structure interaction problems based on computational fluid dynamics (CFD) tools. Here, the aim is to characterize the effect of variabilities in the operating conditions when the aerodynamic operator is strongly affected by nonlinearities due to transonic effects [7] or dynamic stall effects [8]. For the sake of convenience, the influence of the aeromechanical coupling is often neglected in this case.

Probabilistic CFD methods are increasingly used for uncertainty quantification of incompressible flow simulations due to inherent random parameter [9–12]. But very few papers deal with stochastic compressible flows. Such studies are particularly problematic because strong nonlinearities and discontinuities associated with the compressible flow features are reported in the uncertain probabilistic space. Mathelin et al. [13] have applied the Galerkin polynomial chaos (PC) representation to quasi-one-dimensional supersonic nozzle flow with uncertainty in inlet conditions and geometry. For this problem, they have proposed to map their probabilistic space to a substitute space in which they perform a Lagrange interpolation. However, this collocation technique, though reducing the computational burden associated with high-order nonlinearities, downgrades the accuracy of the representation. Some work in the supersonic regime has also been performed by Lin et al. [14] dealing with 2-D Euler equations for a stochastic wedge flow (random inflow velocity and random oscillations of the wedge around its apex). They use a multi-element generalized polynomial chaos method with Legendre polynomial basis and uniform distributions to solve the two-dimensional stochastic Euler equations. A Galerkin projection is employed in the random space and weighted essentially non-oscillatory discretization is used in the physical space. Their analysis shows that the shock wave stochastic response can induce important changes in the mean-flow structure. More recently, Poëtte et al. [12] have proposed a stochastic intrusive approach to tackle shocks in compressible gas dynamics. Their generalized polynomial chaos (gPC)-based technique relies on the decomposition of the entropic variable of the flow and does not require a special discretization of the random space. They have applied their technique to the case of the Sods shock-tube problem with uncertainty carried on the initial interface position between the light and the heavy fluid. Hosder et al. [15] have treated the cases of inviscid shock wave and expansion wave problems with geometric uncertainty and the case of a laminar boundary-layer flow over a flat plate with uncertain viscosity. In all cases, the uncertainty was modeled as a single Gaussian random variable and Hermite polynomials were chosen for the chaos basis. The accuracy of their point-collocation nonintrusive polynomial chaos method applied to multiple uniform random variables has been studied in Hosder et al. [16]. Loeven et al. [7] have made use of a deterministic compressible Reynolds-averaged Navier–Stokes (RANS) code that is coupled to a probabilistic collocation solver to

Received 8 December 2008; revision received 10 December 2009; accepted for publication 12 January 2010.

*Assistant Professor, Institut Jean Le Rond d'Alembert, Case 161, 4 Place Jussieu, Unite Mixte de Recherche 7190.

†Research Associate, Institut Jean Le Rond d'Alembert, Case 161, 4 Place Jussieu, Unite Mixte de Recherche 7190; Université Pierre et Marie Curie, 75005 Paris, France.

propagate freestream aerodynamic (Mach number) uncertainty through a subsonic steady flow around a NACA0012 airfoil. The Mach number takes a uniform distribution form with a 5% coefficient of variation and the angle of attack is deterministic, $\alpha = 5$ deg. The stochastic solution converges fast and exhibits no spatial discontinuity.

In this study, deeper investigations on the stochastic flow around a NACA0012 are proposed for the propagation of multiple aerodynamic uncertainties through transonic flows with possibly separated shear layers. The uncertain parameters under consideration in the numerical simulations are the freestream Mach number and the angle of attack. The variability of these parameters can be attributed to inherent randomness due to freestream turbulence and/or aeroelastic deformations of the structure. The objective of this work is twofold. First, we intend to demonstrate the efficiency and robustness, as well as to point to the limitations, of the nonintrusive stochastic projection approach of uncertainty quantifications with flows presenting shock waves and separation regions. Second, we intend to highlight the potential importance of considering multiple uncertainties, with possibly different random distributions, on the stochastic response of the system. Stochastic results are analyzed in detail by means of various postprocessing of the stochastic aerodynamic field, including error bars, probabilistic density function, sensitivity analysis by means of Sobol's coefficients, and covariance.

II. Uncertainty Quantification Methodology

Classic approaches for stochastic differential equations include Monte Carlo (MC) methods that collect ensemble solution realizations for prescribed ensemble random inputs. Although the convergence rate of MC is slow, it is very convenient, as it only requires running the deterministic solver repetitively and does not depend on the stochastic dimensionality of the problem. Several sampling techniques have been developed to speed up the convergence rate, but ideally, one would like to achieve faster convergence while keeping MC flexibility. Some recent nonintrusive stochastic methods seem to be good alternatives to MC methods.

A. Nonintrusive Stochastic Methods

Let us first make a finite-dimensional noise assumption that allows us to represent our stochastic solution process parametrically through a finite set of N random variables [17]. We define $\boldsymbol{\Theta} = \{\Theta_j(\omega)\}_{j=1}^{N}$ ($N \in \mathbb{N}$) to be a $\mathbb{R}^N$-valued random array on a probability space $(\Omega, \mathcal{A}, \mathcal{P})$ with probability distribution $P_{\boldsymbol{\Theta}}(\mathrm{d}\boldsymbol{\theta})$, where $\mathrm{d}\boldsymbol{\theta} = \mathrm{d}\theta_1, \ldots, \mathrm{d}\theta_N$ is the Lebesgue measure on $\mathbb{R}^N$.

The solution that we seek is a spatial random process u of the random event $\omega \in \Omega$. We can write

$$u(\boldsymbol{x}, \omega) \approx u(\boldsymbol{x}, \Theta_1, \Theta_2, \ldots, \Theta_N) = h(\boldsymbol{x}, \boldsymbol{\Theta})$$

where h: $\boldsymbol{\theta} \mapsto h(\boldsymbol{\theta})$ is a measurable mapping from $\mathbb{R}^N \mapsto \mathbb{R}$. In the following, we will only consider second-order random fields, i.e., such that

$$\mathbb{E}\{\|u\|^2\} = \mathbb{E}\{\|h(\boldsymbol{\Theta})\|^2\} = \int_{\mathbb{R}^N} \|h(\boldsymbol{\Theta})\|^2 P_{\boldsymbol{\Theta}}(\mathrm{d}\boldsymbol{\theta}) < +\infty \qquad (1)$$

where $\mathbb{E}$ denotes the expectation.

We also assume that the components of $\boldsymbol{\Theta}$ are mutually independent, thus building our approximation functional spaces with tensor-product rules and writing the joint probability density function (pdf) $f_{\boldsymbol{\Theta}}$ as a product of the individual pdf, named f_{Θ_j}:

$$f_{\boldsymbol{\Theta}}(\boldsymbol{\theta}) = \prod_{j=1}^{N} f_{\Theta_j}(\theta_j) \qquad (2)$$

However, the f_{Θ_j} do not need to belong to the same type of distribution (cf. mixed distributions).

1. Probabilistic Collocation Method

Collocation methods for the solution of differential and integral equations are based on polynomial interpolations of the solution. The probabilistic collocation method was first introduced by Tatang et al. [18] and has also been described by others [17,19]. In this approach, a nodal set of $N_c + 1$ collocation points is defined in the N-dimensional random space $\Gamma \in \mathbb{R}^N$, where

$$\Gamma \equiv \prod_{j=1}^{N} \Gamma_j$$

and $\Gamma_j \equiv \theta_j(\Omega)$. After collocation projections, the resulting set of deterministic equations is always uncoupled. The solution for each collocation point of the set is obtained via the deterministic solver. The solution u_P is approximated by interpolation on the data points using multidimensional tensor-product Lagrange basis:

$$u_P(\boldsymbol{x}, \boldsymbol{\Theta}) = \prod(u(\boldsymbol{x}, \boldsymbol{\Theta})) = \sum_{k=0}^{N_c} u(\boldsymbol{x}, z_k) L_k(\boldsymbol{\Theta}) \qquad z_k \in \Gamma \quad (3)$$

where the z_k are the collocation points, and the Lagrange polynomials satisfy $L_i(z_j) = \delta_{ij}$ for $0 \le i, j \le N_c$. The complexity of the Lagrange basis (for $N > 1$) makes it difficult to extract realizations or generate the pdf of the random process. That is why most of the research work focuses mainly on the solution moments, which requires only integrating those Lagrange interpolation polynomials:

$$\mathbb{E}\{u_P(\boldsymbol{x}, \boldsymbol{\Theta})\} = \sum_{k=0}^{N_c} u(\boldsymbol{x}, z_k) \int_{\Gamma} L_k(\boldsymbol{\theta}) f_{\boldsymbol{\Theta}}(\boldsymbol{\theta})\, \mathrm{d}\boldsymbol{\theta} \qquad (4)$$

which can be quite cumbersome for large N, unless one chooses the nodal set of collocation points to be a set of cubature points [17]. So in practice, the moments are not available for any given choice of points. Another drawback is the interpolation error of Eq. (3), which is hard to control, because uniformly bounded by a quantity that depends on the choice of the nodal set. Finally, it should be mentioned that if no particular care is taken to construct the space of approximations, the method is likely to suffer from the "curse of dimensionality" [19].

2. Stochastic Spectral Projection Method

In this study, we choose to rely instead on the gPC framework [20], which is a generalization of the original homogeneous chaos introduced by Wiener [21] and later developed by Ghanem and Spanos [22] in the context of finite elements.

We consider the following multivariate orthogonal polynomials that are built as tensor products of univariate orthogonal polynomials along each random dimension with respect to the probability measure $P_{\Theta}(\mathrm{d}\boldsymbol{\theta})$:

$$\phi_{\boldsymbol{\alpha}}(\boldsymbol{\theta}) = \phi_{\alpha_1}(\theta_1) \otimes \cdots \otimes \phi_{\alpha_N}(\theta_N)$$

Here, $\boldsymbol{\alpha} = (\alpha_1, \ldots, \alpha_N) \in \mathbb{N}^N$ represents a set of multi-indices. We define the length of $\boldsymbol{\alpha}$ with the following norm: $|\boldsymbol{\alpha}| \equiv \alpha_1 + \cdots + \alpha_N$.

The family of polynomials with total degree not greater than P, i.e., $\{\phi_{\boldsymbol{\alpha}}(\boldsymbol{\theta}) / |\boldsymbol{\alpha}| \le P\}$, and orthogonal with respect to $P_{\Theta}(\mathrm{d}\boldsymbol{\theta})$, that is,

$$\mathbb{E}\{\phi_{\boldsymbol{\alpha}}(\boldsymbol{\Theta}) \phi_{\boldsymbol{\beta}}(\boldsymbol{\Theta})\} = \mathbb{E}\{\phi_{\boldsymbol{\alpha}}^2(\boldsymbol{\Theta})\} \delta_{\boldsymbol{\alpha}\boldsymbol{\beta}} \qquad (5)$$

are used as a basis of the gPC representation of u,

$$u(\boldsymbol{x}, \boldsymbol{\Theta}) = \sum_{\boldsymbol{\alpha} \in \mathbb{N}^N} \hat{u}_{\boldsymbol{\alpha}}(\boldsymbol{x}) \phi_{\boldsymbol{\alpha}}(\boldsymbol{\Theta}) \qquad (6)$$

with its deterministic coefficients computed from

$$\hat{u}_{\boldsymbol{\alpha}}(\boldsymbol{x}) = \mathbb{E}\{u(\boldsymbol{x}, \boldsymbol{\Theta}) \phi_{\boldsymbol{\alpha}}(\boldsymbol{\Theta})\} / \mathbb{E}\{\phi_{\boldsymbol{\alpha}}^2(\boldsymbol{\Theta})\} \quad \text{for } \boldsymbol{\alpha} \in \mathbb{N}^N \qquad (7)$$

In practice, the order P is chosen based on accuracy requirements. The multi-index $\boldsymbol{\alpha}$ can be renumbered with a unique index and the cardinality of the corresponding set is given by

$$Q = \binom{N+P}{P}$$

The gPC representation with Q terms reads

$$u(\boldsymbol{x}, \boldsymbol{\Theta}) = \sum_{j=0}^{Q-1} \hat{u}_j(\boldsymbol{x})\phi_j(\boldsymbol{\Theta}) \tag{8}$$

This method is nonintrusive in the sense that we perform a Galerkin projection of the stochastic solution directly onto each member of the orthogonal basis. It has the advantage of not requiring modifications to the existing deterministic solver. The evaluation of the unknown coefficients is equivalent to computing multidimensional integrals. In our case, the gPC coefficients are evaluated through numerical quadrature that will be described in the next section.

It is worth mentioning that the optimal choice of the gPC basis remains an open question. Indeed, the type of distribution of the stochastic partial-differential-equation solution is not known most of the time. When the random input distribution is known, one can choose the corresponding polynomial from the Askey family as the gPC basis [20]. However, the optimality is only guaranteed for the stochastic inputs. In particular, for nonlinear problems, it is not clear that an optimal representation of the inputs is necessarily optimal for the entire problem. Numerical accuracy of the final representation is assessed in Appendices A, B, and C. In particular, the interplay between the stochastic and the spatial discretizations are addressed in those sections.

Once the modal coefficients are computed, moments, sensitivity analysis, confidence intervals, and pdf of the solution can be evaluated. Because of the orthogonality of the modes, the moments can be easily computed. For instance, the computation of the covariance R_{uv} between two random fields $u(\boldsymbol{x}, \boldsymbol{\Theta})$ and $v(\boldsymbol{x}, \boldsymbol{\Theta})$ becomes

$$R_{uv}(\boldsymbol{x}_1, \boldsymbol{x}_2) = \mathbb{E}\{u(\boldsymbol{x}_1, \boldsymbol{\Theta}) - \mathbb{E}\{u(\boldsymbol{x}_1, \boldsymbol{\Theta})\}, v(\boldsymbol{x}_2, \boldsymbol{\Theta}) - \mathbb{E}\{v(\boldsymbol{x}_2, \boldsymbol{\Theta})\}\} = \sum_{j=1}^{Q-1} \hat{u}_j(\boldsymbol{x}_1)\hat{v}_j(\boldsymbol{x}_2)\mathbb{E}\{\phi_j^2\} \tag{9}$$

The sensitivity analysis is carried out by means of the analysis of Sobol's coefficients [23]. The computation of these coefficients becomes trivial when the stochastic solution is decomposed onto its associated gPC basis. In this case, the hierarchical nature of the gPC representation is another advantage compared with the Lagrange interpolation. Concerning the computation of the pdf of the response, several approaches are conceivable. One simple way to proceed is to generate a large population sample since Eq. (8) involves only algebraic evaluations with little computational cost. An histogram of these data can then be built. A variant that produces smoother distributions is the kernel-smoothing density estimate [24] that we use in this study.

B. Numerical Implementation

In this work, due to the choice of uniform and/or truncated Gaussian distributions for the inputs and without any a priori knowledge of the outputs pdf solution, appropriate basis functions from a mathematical point of view are the Legendre polynomials (uniform) [20], the Jacobi polynomials (beta) [25], or the Legendre–Jacobi mixed polynomial basis.

1. Standard Gauss-Quadrature Formula

Different ways of dealing with high-dimensional integrations of Eq. (7) can be considered, depending on the prevalence of accuracy versus efficiency [26]. An accurate approximation consists of numerical Gauss-quadrature evaluated for some chosen points, but this approach is too costly for large N. An alternative is sparse quadratures [27], which require less quadrature points. The sparse quadrature based on the Smolyak algorithm [28] has the advantage of remaining accurate, with a convergence rate depending weakly on N. However, the standard isotropic version, such as the Smolyak–Clenshaw–Curtis, does not perform well for anisotropic problems, i.e., when the solution is more sensitive to one of the random dimensions, which is the case in this study. We prefer to use numerical quadratures of Gauss type by full-tensor products, as our number of random dimensions is small (at most, $N = 2$). Based on polynomial accuracy, we use a minimum number of $(P+1)^N$ quadrature points for the estimation of all Q coefficients.

2. Extended Gauss-Quadrature Formula

The numerical cost of the Gauss quadrature is related to the number of collocation points of the one-dimensional grids before the tensorization. When the grid is refined, one would ideally like to keep the previous simulation results in order to improve the prediction. Unfortunately, this is not achievable with traditional Gauss quadratures, for which successive grid levels do not share any collocation points. One way to optimally enrich our collocation grids is to consider nested one-dimensional grids.

For one-dimensional integration, Kronrod [29] has proposed to extend a n_q-point Gauss-quadrature rule by interlacing $m_q = (n_q + 1)$ new points with positive weights. The degree of polynomial exactness of the $(n_q + m_q)$-point integration rule becomes $p = 3n_q + 1$ (for even n_q) and $p = 3n_q + 2$ (for odd n_q). Patterson [30] has generalized this approach by a recursive expansion of Kronrod's [29] scheme. In the following, the computation of the additional m_q Kronrod quadrature points location for a given initial n_q-Legendre points grid, as well as the computation of the corresponding weights, are obtained via Laurie's algorithm [31] and Gautschi's implementation [32].

For multidimensions, it is interesting to compare the cost of Kronrod grids obtained by full-tensor products with the standard Gauss-quadrature grids. Let us consider the case at integration level l, where we have already performed $N_q^l = (n_q)^N$ (with n_q even) simulations and wish to refine our quadrature grid. When building a Kronrod grid by adding m_q points along each direction, the additional cost at the new stage becomes

$$N_q^{l+1} = (n_q + m_q)^N - N_q^l = (2n_q + 1)^N - n_q^N$$

This guarantees a polynomial degree of exactness of $p = 3n_q + 1$. The same accuracy can be obtained by performing simulations on a completely new standard Gauss-quadrature grid with $N_q^{l+1} = ((3n_q + 1)/2 + 1)^N$ points.

In Table 1, we determine the prevalence in terms of cost of Kronrod-vs-Gauss types of quadrature enrichment in $N = 1$ and 2 dimensions. We conclude that if Kronrod is always less expensive in $N = 1$, then in $N = 2$ dimensions, it is less expensive or comparable for $n_q < 3$. For $N > 2$, the Kronrod grid is not a good choice anymore. For higher dimensions, it is in fact more efficient to construct the Kronrod grid with a sparse collocation technique such as the Smolyak algorithm [33].

III. Stochastic Transonic Flows Past an Airfoil

In this section, the nonintrusive stochastic collocation formulation is applied to the propagation of several aerodynamic uncertainties through a transonic steady flow around a NACA0012 airfoil. The CFD solver that is used to compute the deterministic flow solutions is described in Sec. III.A. The stochastic analysis with combined effects from freestream Mach number and angle of attack is presented

Table 1 Additional cost, i.e., number of additional quadrature points to add to an existing $(n_q)^N$-point grid, in order to reach a polynomial accuracy of $p = 3n_q + 1$ (here, n_q is even)

Dimension	Gauss	Kronrod	n_q range[a]
$N = 1$	$\frac{3}{2}(n_q + 1)$	$n_q + 1$	$n_q > 0$
$N = 2$	$\frac{9}{4}(n_q + 1)^2$	$3(n_q + 1)^2 + 2(n_q + 1)$	$n_q < 3$

[a]Denotes the n_q bound for which the Kronrod approach is less expensive.

in Sec. III.B, with emphasis to the presentation of the stochastic flow model, the analysis of the results obtained for uniform random distributions, and the extension to nonuniform distributions. Appendices A, B, and C are devoted to the discussion of spatial and stochastic requirements and convergence analysis of the gPC formulation.

A. Deterministic Flow Computations

The deterministic steady-state flow solutions are computed using a Favre–Reynolds-averaged Navier–Stokes solver and a near-wall wall-normal-free Reynolds-stress model (RSM) [34,35]. The governing equations are discretized using a $\mathcal{O}(\Delta x^3)$ finite volume upwind-biased MUSCL scheme, and the time integration is based on an implicit dual-time-stepping procedure with alternating-direction implicit subiterations [36]. This solver has been validated for various steady and unsteady flow configurations [34,36,37] and is particularly suited for the parametric computations involved in this study. All computations performed in this work were obtained using the following Courant–Friedrichs–Lewy (CFL) numbers: CFL $= 100$ for the time step and CFL$^* = 10$ for the dual pseudo time step. The number of subiterations is chosen dynamically, based on the reduction of the error between two subiterations by a factor $r_{\mathrm{MF}} = 1.5$. A complete description of the pseudo-time-implicit dual-time-stepping algorithm can be found in Chassaing et al. [36].

The computational mesh is based on a structured O-grid with 301 grid points around the airfoil and 151 points in the radial direction [37]. The chord of the airfoil is $c = 0.1$ m and the far-field boundary was placed at a distance $d = 20c$ from the airfoil. The minimum nondimensional grid spacing at the wall is $y_w^+ < 0.3$. A geometric progression ratio of $r_j = 1.35$ is used to stretch the computational grid in the radial direction, and the geometric progression ratio used near the leading edge and the trailing edge are, respectively, $r_{i_{\mathrm{LE}}} = 1.16$ and $r_{i_{\mathrm{TE}}} = 1.3$. At the far field, the total temperature was imposed to $T_{t_\infty} = 280$ K and the total pressure was imposed to $p_{t_\infty} = 382,197.9$ Pa. The turbulence intensity T_{u_∞} and the turbulence-length scale ℓ_{T_∞} were, respectively, set to $T_{u_\infty} = 0.8\%$ and $\ell_{T_\infty} = 0.1$ m.

B. Combined Freestream Mach Number and Angle-of-Attack Uncertainties

1. Stochastic Flow Model

In this study, the stochastic flow model is based on the uncertainty propagation of two random disturbances associated with the angle of attack α and the freestream Mach number M_∞. These two parameters were selected because they are classically used in the context of robust design of airfoils. It is obvious that from the point of view of aeroelastic investigations, the choice of these uncorrelated variables results in a crude model, since no aeromechanical coupling is assumed.

A critical point that arises when dealing with uncertainty quantifications is how to model the uncertain parameters by carefully choosing the support of their random distributions. Although different distributions for different parameters are not incompatible with the gPC formulation, we prefer to first consider uniform distributions for both parameters. This choice means that we do not favor any particular parametric value within the domain of interest. Moreover, the choice of a uniform distribution is justified, as it is the maximum entropy distribution for any continuous random variable on an interval of compact support. In other words, an assumption of any other prior distribution satisfying the constraints will have a smaller entropy, thus containing more information and less uncertainty than the uniform distribution [38]. Hence, considering $\boldsymbol{\Theta} = [\Theta_1(\omega), \Theta_2(\omega)]^T$, where Θ_1 and Θ_2 are associated with α and M_∞, respectively, any aerodynamic variable $q(\mathbf{x}, \Theta_1, \Theta_2)$ is then approximated with the gPC representation by the following expansion:

$$q(\boldsymbol{x}, \Theta_1, \Theta_2) = \sum_{j=0}^{Q-1} \hat{q}_j(\boldsymbol{x}) \phi_j(\Theta_1, \Theta_2) \tag{10}$$

The input random variables are defined with their mean values μ and standard deviations σ:

$$\alpha = \mu_\alpha + \sigma_\alpha \Theta_1 \qquad M_\infty = \mu_{M_\infty} + \sigma_{M_\infty} \Theta_2 \tag{11}$$

The corresponding standard deviations of the uncertain parameters are $\sigma_\alpha = 1$ deg and $\sigma_{M_\infty} = 0.05$. The range of α is representative of typical amplitudes of static deformations observed on flexible wings with a NACA0012 section at similar operating points [39,40]. The variation interval of the freestream Mach number ($M_\infty = \mu_{M_\infty} \pm 0.05$) is relevant to typical operating ranges used for the study of robust shape optimization problems [41,42]. In the present study, a parametric stochastic analysis was conducted using different mean values of the uncertain parameters α and M_∞. These conditions are reported in Table 2. As a consequence, the global parametric range covered by the four stochastic flow regimes corresponds to $2 \text{ deg} \le \alpha \le 6$ deg and $0.5 \le M_\infty \le 0.7$. The corresponding Reynolds number range is $4.1 \times 10^6 \le Re \le 5.2 \times 10^6$.

The first configuration (namely, case A) corresponds to highly subsonic flow conditions at low incidence ($\mu_\alpha = 3$ deg and $\mu_{M_\infty} = 0.55$). The next two stochastic operating ranges (case B and case C) are likely to include shock wave effects at moderate angle of attack (case B, $\mu_\alpha = 5$ deg, and $\mu_{M_\infty} = 0.55$) or at higher Mach number (case C, $\mu_\alpha = 3$ deg, and $\mu_{M_\infty} = 0.65$). Finally, case D ($\mu_\alpha = 5$ deg and $\mu_{M_\infty} = 0.65$), is likely to include flow realizations with a separated shear layer on the suction side of the airfoil in addition to shock waves. Each stochastic computation was performed using $n_q = 8$ Gauss–Legendre quadrature points per random dimension. The corresponding stochastic $n_q \times n_q$ grids of the uncertain parameter space (α, M_∞) are shown in Fig. 1.

Note also that because we are interested in steady flows only, the airfoil is not subject to forced or self-sustained aeroelastic motions such as flutter. Furthermore, we have checked that the present operating range excludes the buffet boundary of the NACA0012 airfoil identified experimentally by Bartels [43] for the same range of Reynolds numbers (Fig. 1).

2. Analysis of the Stochastic Flows for Uniform Distributions

The physical analysis of the stochastic flow response is now presented. The following results were obtained using a seventh-order gPC expansion (i.e., $P = 7$). We refer the reader to Appendices A, B, and C for the motivation behind this choice.

The first two statistical moments of the lift and drag forces are summarized in Table 3 for the four stochastic flow regimes depicted in Table 2. Here, the mean and the coefficient of variation (COV$= \sigma/\mu$) of the lift-to-drag L/D ratio are chosen as representative indicators of the global aerodynamic performance of the airfoil. One may note in Table 3 that the stochastic conditions of highest efficiency (case C, $\alpha = 3$ deg and $M_\infty = 0.55$) correspond to the lowest sensitivity level of L/D due to the input uncertainties. As expected, case D ($\alpha = 5$ deg and $M_\infty = 0.65$) exhibits the minimum

Table 2 Characteristics of the studied stochastic flow regimes based on uncertain angle of attack and freestream Mach number

Case	μ_α, deg	σ_α, deg	Θ_1	μ_{M_∞}	σ_{M_∞}	Θ_2	Dominant flow regime
A	3	1	Uniform	0.55	0.05	Uniform	High subsonic
B	3	1	Uniform	0.65	0.05	Uniform	Transonic
C	5	1	Uniform	0.55	0.05	Uniform	Transonic
D	5	1	Uniform	0.65	0.05	Uniform	Transonic with separation

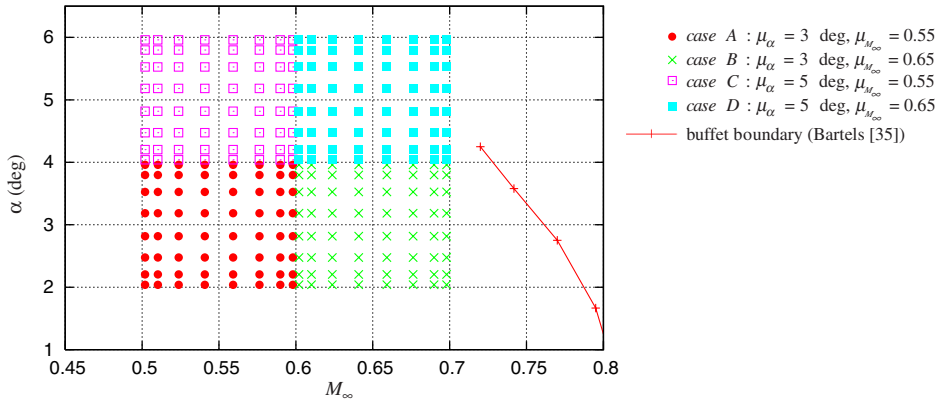

Fig. 1 Gridding of the aerodynamic (α, M_∞) parameter space corresponding to the four stochastic flows described in Table 2 and buffet boundary of the NACA0012 airfoil [43]. The computational grid totals up to 4 × 64 RSM-RANS simulations.

value of $\mu_{L/D}$, but in conjunction with the highest variability level, therefore making it the most challenging case.

Figure 2 shows the mean and the standard deviation of the Mach number computed for case D. The mean Mach number field is illustrated in Fig. 2a. We note that shock discontinuities are smoothed out due to the uncertainty. It then becomes impossible to distinguish the discontinuities associated with the shock waves, resulting in substantial modifications of the mean value of the solution.

The sensitivity of the shock response to the input uncertainty is confirmed by the examination of the variance of the Mach number σ_M^2, as shown in Fig. 2b, in which important variations are observed on the upper side of the airfoil for $1/6 \leq x/c \leq 1/4$. The maximum of σ_M^2 is located near the airfoil surface around the first quarter of the chord. This uncertain region is related to the effects of the aerodynamic nonlinearities associated with the interaction between the shock wave and the turbulent boundary-layer. However, one can also note that the edge of the turbulent boundary layer is sensitive to the input random parameters, but no variations are observed either on the pressure side or in the wake of the airfoil. Since we use a nonintrusive gPC formulation coupled with a RSM-RANS solver, the prediction of the stochastic response of the turbulent field is straightforward. It can be seen from Fig. 3 that the regions of sensitivity of the turbulent field strongly differs between the normal Reynolds-stress components $\widetilde{u''u''}$ and $\widetilde{v''v''}$.

Next, the stochastic results were analyzed by means of the uncertainty bars of the isentropic Mach number M_{is} distribution along the airfoil surface:

$$M_{\text{is}}(p, p_{t_\infty}) = \sqrt{\frac{2}{\gamma - 1}\left[\left(\frac{p_{t_\infty}}{p}\right)^{\frac{\gamma-1}{\gamma}} - 1\right]} \tag{12}$$

where p denotes the static pressure. Figure 4 displays the M_{is} confidence intervals for each stochastic flow regime. Both standard-based confidence intervals and full confidence intervals are included. Full confidence intervals coincide with the supports of the pdf of the response (pdf results are presented next). For the sake of clarity, only the distributions along the upper airfoil surface are presented.

One may note from the results of case A that the maximum M_{is} mean value on the airfoil is $\mu_M = 0.9$, and all flow realizations within the interval $\mu_M \pm \sigma_M$ correspond to subsonic conditions. However, this is not the case if we look at the full interval of confidence, which includes transonic flow realizations (with shocks up to $M_{\text{is}} = 1.19$) as well. As already observed by Loeven et al. [7], the flow region characterized by an important level of variation is located on the upper surface of the airfoil near the leading edge. We note that for this case, the position giving the highest flow sensitivity level coincides with the position of the maximum value of $\mu_{M_{\text{is}}}$ ($x/c = 0.02$). After this position, the amplitude of the error bar decreases smoothly down to the trailing edge. Keeping the range of the freestream Mach number ($0.5 \leq M_\infty \leq 0.6$) unchanged but increasing the angle of attack up to $\alpha = 5$ deg results in much larger variations of the stochastic flowfield, as shown in Fig. 4 (case C). Consequently, the statistical response of the isentropic Mach number on the airfoil surface is now clearly separated into two distinct regions:

1) The flow on the part of the airfoil limited by $x/c < 0.2$ is characterized by an important sensitivity to the uncertain conditions. These large variations can be attributed to the nonlinear effects of the shock wave. In this case, note that the position of the maximum value of $\mu_{M_{\text{is}}}$ located at $x/c = 0.03$ does not coincide with the maximum of $\sigma^2_{M_{\text{is}}}$.

2) For $x/c > 0.2$, the influence of the shock wave on the stochastic field vanishes and the amplitude of the error bars becomes comparable with those obtained for the subsonic configuration (Fig. 4, case A).

A quite different uncertainty-bar distribution is observed in the results of case B ($\alpha = 3$ deg, $M_\infty = 0.65$). The region affected by high variabilities extends up to $x/c < 0.4$, which is approximately twice further than those obtained for case C ($\alpha = 5$ deg and $M_\infty = 0.55$). Finally, the region of sensitivity computed for case D ($\alpha = 5$ deg and $M_\infty = 0.65$; Fig. 4, case D) is relatively similar to those obtained with $\mu_\alpha = 5$ deg (case C). A possible explanation is that when the flow is dominated by a separated shear layer, the stochastic motion of the shock wave in the direction toward the trailing edge is restrained by the separation bubble for which the position of the separating point is practically independent of the angle of attack.

Richer statistical information is obtained by considering the pdf of the solution, which was computed using 10,000 samples. Figure 5 shows the normalized pdf of the isentropic Mach number on the suction side of the airfoil for the different stochastic flow conditions.

The pdf contours are normalized at each streamwise location such that the maximum probability density is always unity. This is done because we are more interested in the distribution of the strongest gradients and most probable solutions than in the pdf amplitudes.

Keeping in mind that the aerodynamic uncertainties on α and M_∞ were modeled using uniform random distributions, it is interesting to note that the pdfs of the stochastic solution are not uniform in some regions. This is the signature of the system nonlinearity. Considering, for instance, the results of case A ($\alpha = 3$ deg and $M_\infty = 0.55$), we remark that uniform pdfs of the flow response are only observed for $x/c > 0.5$. but not for the upward region, which presents large variations of the stochastic solution.

Table 3 Statistical moments (mean and standard deviation) of the lift and drag forces and (mean and coefficient of variation: COV = σ/μ) of lift-to-drag ratio C_l/C_d obtained for the four stochastic flows described in Table 2

Case	μ_L, N	σ_L(N)	μ_D, N	σ_D, N	μ_{C_l/C_d}	COV_{C_l/C_d}, %
A	2651	592	70	7	37.6	15.6
B	3847	825	106	30	36.9	14.2
C	4397	678	88	18	50.5	6.8
D	5989	628	229	102	30.3	32.9

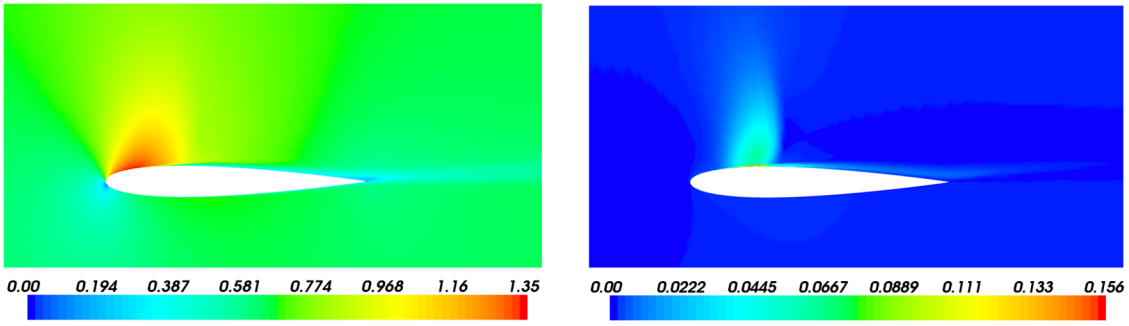

a) Mach number: μ_M b) Mach number: σ_M^2

Fig. 2 Mean and variance of the Mach number field computed from a sixth-order gPC expansion (case D, $\mu_\alpha = 5$ deg and $\mu_{M_\infty} = 0.65$).

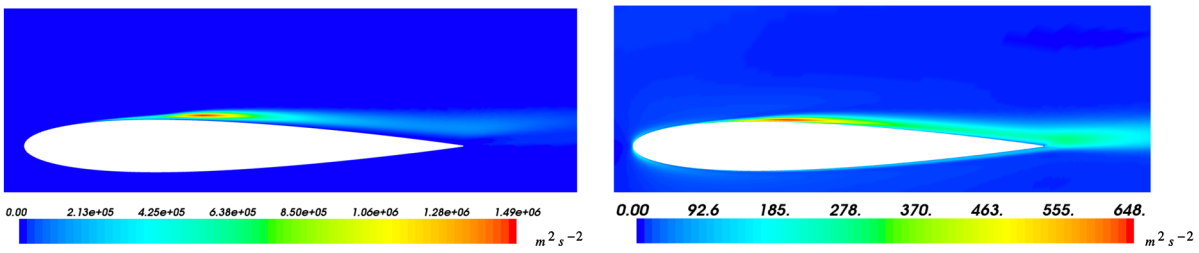

a) Variance: $\widetilde{u''u''}$ b) Variance: $\widetilde{v''v''}$

Fig. 3 Variance of the Reynolds-stress components computed from a seventh-order gPC expansion (case D, $\mu_\alpha = 5$ deg and $\mu_{M_\infty} = 0.65$).

At transonic conditions (Fig. 5, case B and case C), the pdf of M_{is} can lead to very complex distributions in the regions characterized by nonlinear effects. More surprisingly, it can be clearly observed in the results of case D ($\alpha = 5$ deg and $M_\infty = 0.65$) that the pdf of M_{is} exhibits a double peak around the position $x/c = 2.2$. The existence of a such bifurcation is probably due to the combined effects of the shock wave and the separated shear layer. Contour plots for cases B and C hint at a somewhat similar jump in the solution, with a most probable value quickly switching from a larger to a lower value. This phenomenon takes place at around $x/c \approx 0.12$ for case B and at around $x/c \approx 0.05$ for case C. Note also that the distribution of the pdf near the trailing edge of case D is slightly modified compared

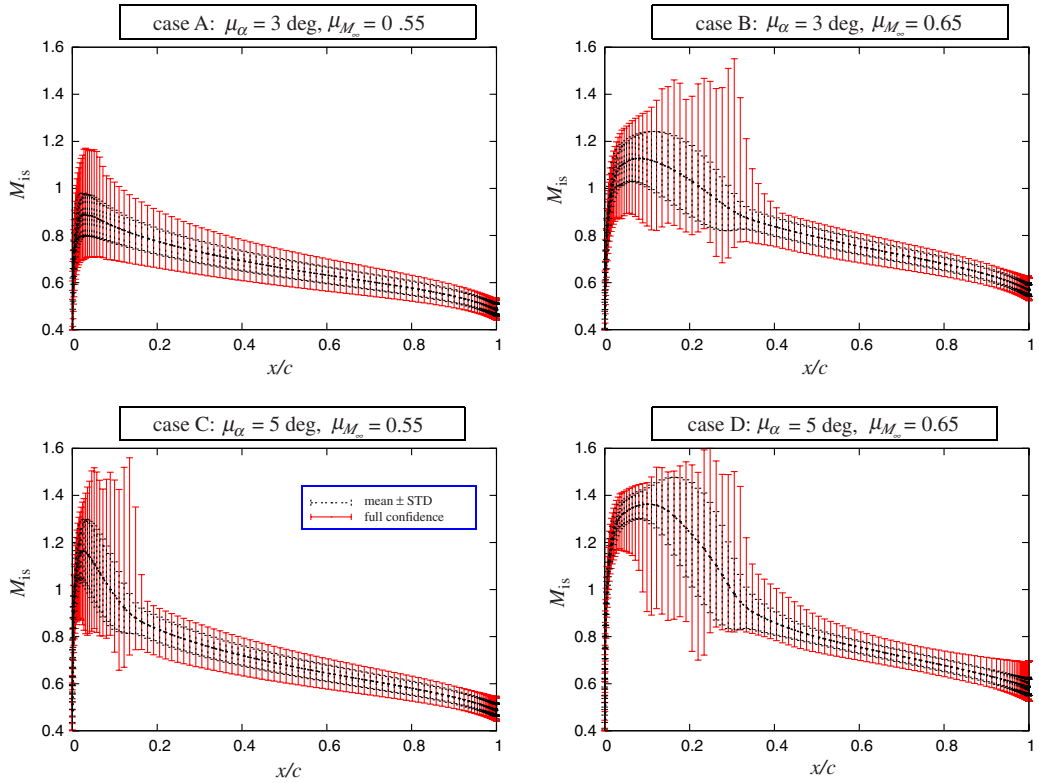

Fig. 4 Steady–state isentropic Mach number M_{is} statistical distributions along the upper NACA0012 airfoil surface. Both standard-based and full confidence intervals are represented together with the mean distributions.

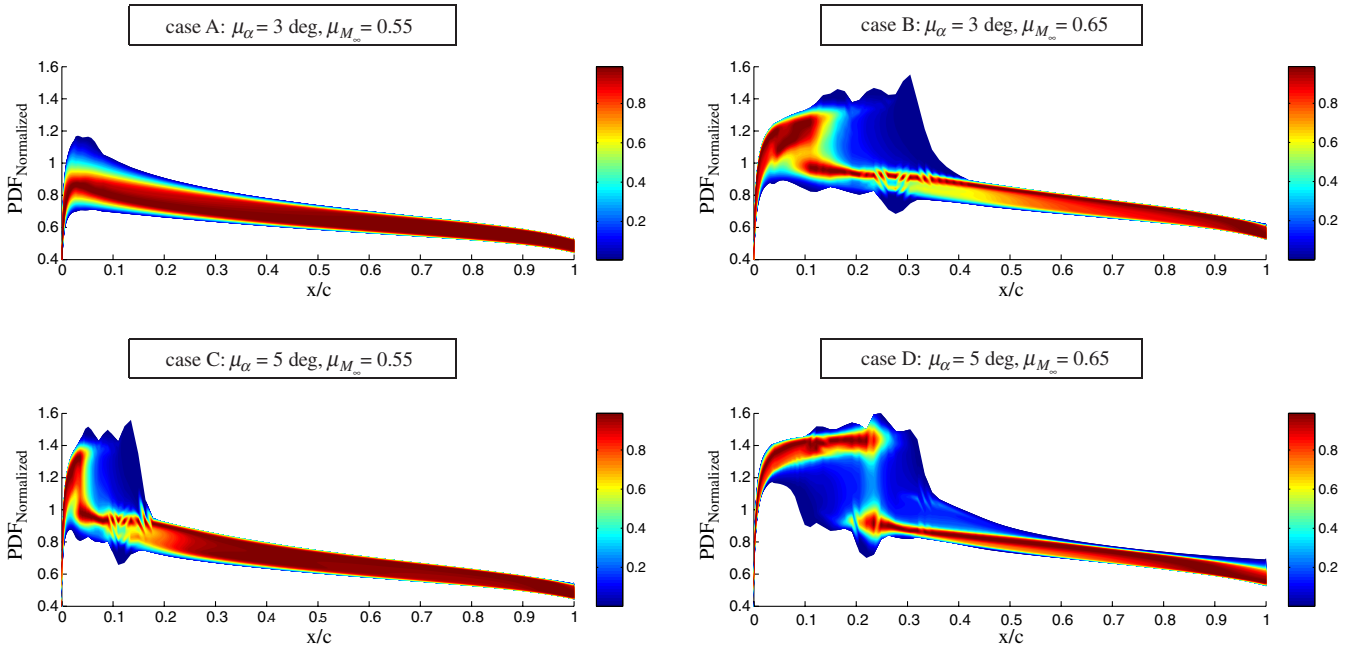

Fig. 5 Steady–state isentropic Mach number M_{is} pdfs along the upper NACA0012 airfoil surface.

with the previous cases. It must be noted that the streaks observed for case B at around $x/c \approx 0.3$ and for case C at around $x/c \approx 0.1$ are strongly accentuated due to the rendering of the contour plots on irregularly spaced grids.

Figure 6 shows the confidence intervals and statistics of the skin-friction coefficient C_f along the upper airfoil surface. We observe that the distribution of C_f computed for the subsonic configuration (case A, $\alpha = 3$ deg and $M_\infty = 0.55$) is quite insensitive to the input uncertainty. Nonetheless, at higher freestream Mach number (Fig. 6, case B) or angle of attack (Fig. 6, case C), the confidence interval in the predictions of C_f presents larger variations, particularly along the windward part of the airfoil. These regions of high sensitivity are similar to those observed on the stochastic distributions of M_{is} (Fig. 4). Again, it appears that the results of case D ($\alpha = 5$ deg and $M_\infty = 0.65$) exhibit the largest variations to the stochastic flow.

Another important aspect of the propagation of several uncertainties is to be able to monitor possible coupled effects between the random parameters onto the stochastic response of the system. In the following, we investigate this coupling by means of computing Sobol's coefficients [23]. Those coefficients can be seen as partial variances of M_{is} associated with the uncertain parameters α and M_∞.

Figure 7 shows the sensitivity indices (expressed here in the form of standard quantities) for the four different cases. The results of case A show that the individual contributions of each random

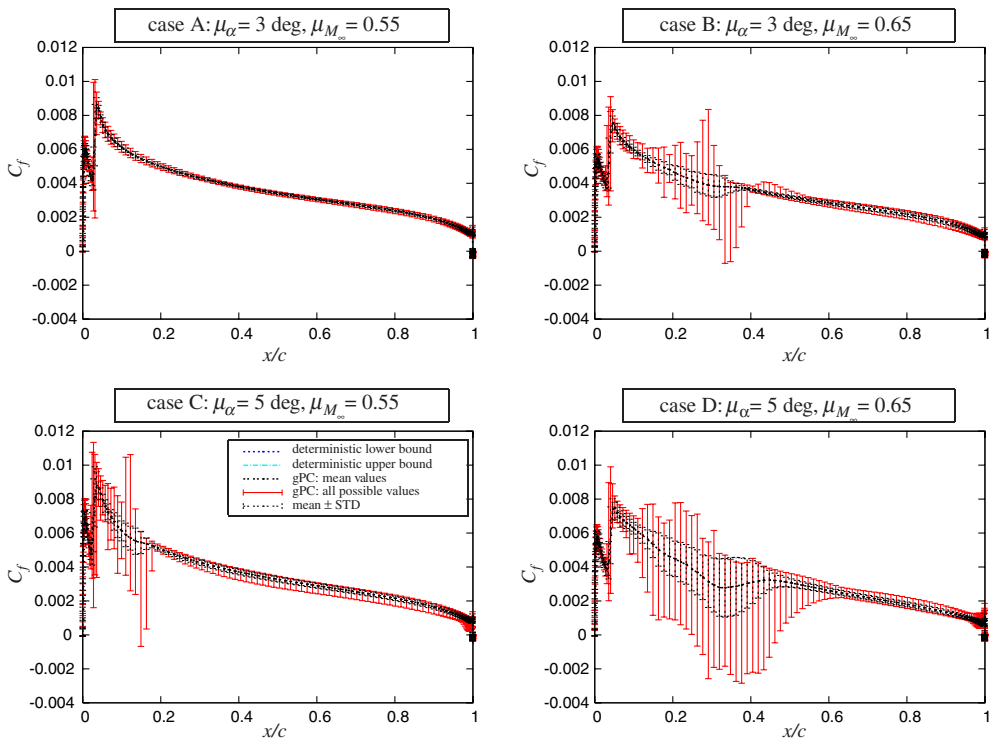

Fig. 6 Steady–state skin-friction C_f statistical distributions along the upper NACA0012 airfoil surface. Both standard-based and full confidence intervals are represented together with the mean distributions.

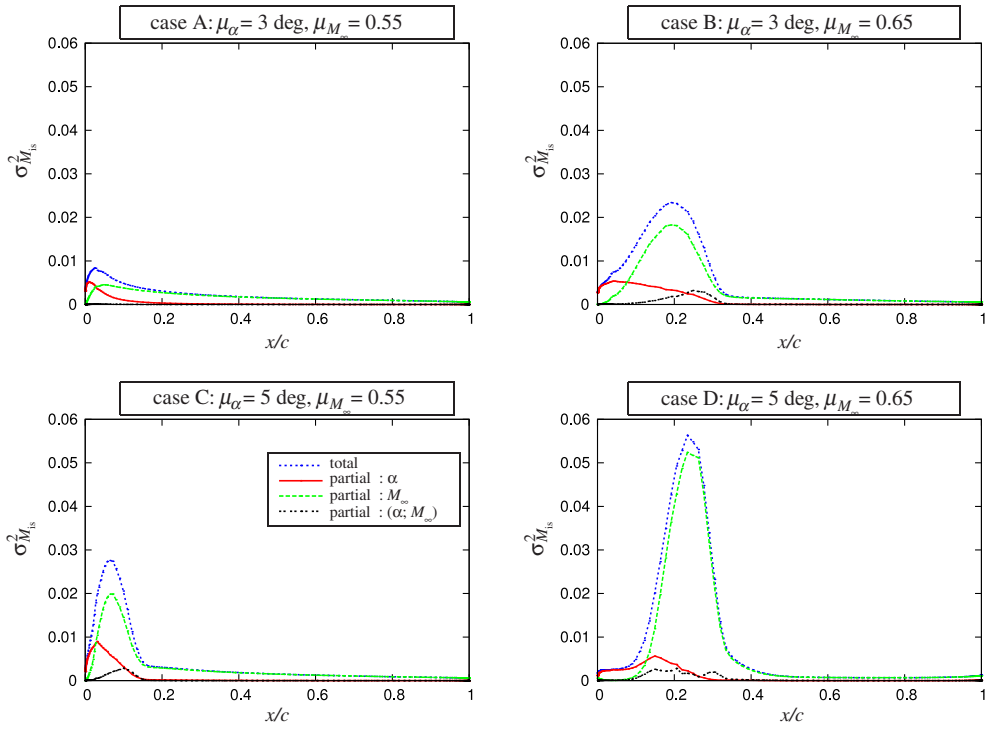

Fig. 7 Steady-state isentropic Mach number M_{is} sensitivity indices along the upper NACA0012 airfoil surface.

variable associated with α and M_∞ have the same order of magnitude but act at different locations along the airfoil surface. In this case, the coupling between the two uncertainties is insignificant. The balance in the contribution of each random variable on the resulting total variance is quite different for cases B and C. It appears that the total variance of M_{is} is mainly dominated by the flow sensitivity to the freestream Mach number (Fig. 7, cases B and C). Moreover, the contribution of the cross terms associated with the coupling of the uncertainties becomes notable, as a consequence of the nonlinear effects. The results of case D ($\alpha = 5$ deg and $M_\infty = 0.65$) confirm that the sensitivity of the stochastic flow to the freestream Mach number is mainly driven by the variabilities due to M_{is}. The influence of the partial variance due to the cross term $\Theta_1\Theta_2$ has the same order of magnitude as those observed for case B and case C, but it covers a larger part of the airfoil (approximately 25% of the surface).

Finally, it is interesting to analyze how the stochastic distributions of C_p and C_f vary together on the upper surface of the airfoil. Figure 8 presents the results of the covariance $R_{C_pC_f}$ [Eq. (9)] for case D. The region where the stochastic distributions of C_p and C_f are highly correlated ranges mainly from the leading edge up to the midchord of the airfoil ($0 \le x/c \le 0.5$). One can also observe that both negative and positive values of R_{CpCf} are obtained. Therefore, the skin friction at a particular location x_1/c and the pressure coefficient at x_2/c can vary together or in an opposite manner. For instance, it appears that the stochastic values of C_p and C_f between the leading edge ($0.04 \le x/c \le 0.06$) and the region defined by $0.2 \le x/c \le 0.4$ are correlated in the same way. Consequently, when one of these two variables is above its expected value, then the second variable will be above its expected value too. A similar behavior is observed for the region defined by $0.2 \le x/c \le 0.4$. However, this region is bounded by two additional regions with negative R_{CpCf}. This means that when one of these variables is above its expected value, the other variable tends to be below its expected value.

As a concluding remark on the physical analysis performed in this section, we note that uniform distributions of uncertain angle of attack and freestream Mach number lead to nonuniform distributions of the aerodynamic coefficients C_p and C_f on the airfoil when the nonlinearities associated with the compressible flow features are reported in the uncertain probabilistic space. In this case, the coupling between these uncertainties becomes nonnegligible (especially for case D, $\alpha = 5$ deg and $M_\infty = 0.65$). In addition, the study of the cross-correlation between C_p and C_f shows that it is possible to identify particular regions on the airfoil surface for which these coefficients may vary together or separately.

3. *Extension to Nonuniform Mixed Distributions*

Here, the impact of nonuniform distributions on the stochastic flow is investigated. The gPC representation has the capability of representing random functional processes for which the underlying random variables have different distributions. Spectral convergence of the gPC representation based on mixed basis was demonstrated for simple stochastic ordinary differential equations [44] (these results are not presented here). In the following, test cases with mixed random distributions are considered. We choose to keep a uniform distribution for α and to assign a truncated Gaussian distribution f_{tG} to M_∞. The latter distribution resembles a Gaussian distribution but

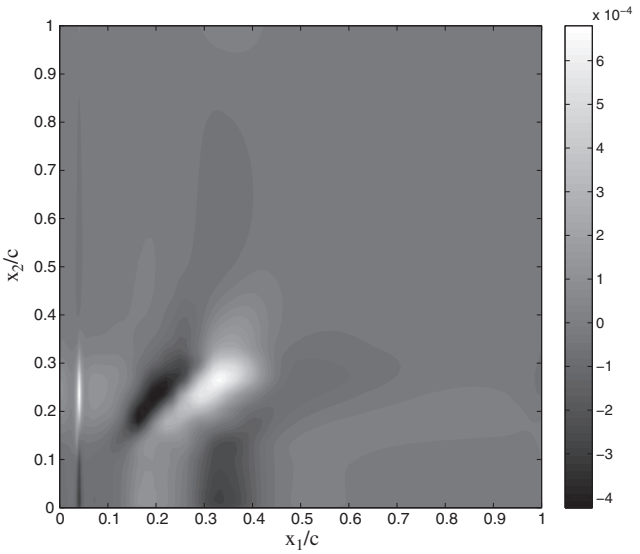

Fig. 8 Cartography of the covariance between the stochastic distributions of the pressure coefficient and the skin-friction coefficient on the upper NACA0012 airfoil surface (case D).

bears truncated tails. Although Gaussian distributions seem a natural choice when the nature of the actual random inputs is unclear, truncated Gaussian distributions are convenient to ensure that negative values of the M_∞ have zero probability of occurrence, i.e., the problem is not ill-posed.

Starting from case D ($\mu_\alpha = 5$ deg and $\mu_{M_\infty} = 0.65$), we have performed $n_q^2 = 8 \times 8$ additional stochastic computations to highlight the effect of the truncated Gaussian distribution

$$f_{tG}(\mu_{M_\infty} = 0.65, \sigma_{M_\infty} = 0.05, a = \min_{M_\infty} \approx 0.5, b = \max_{M_\infty} \approx 0.8)$$

for M_{is}. For the comparison to be fair, the mean and standard of the random parameter are taken the same as previously, whereas the bounds of the distribution (a, b) are accurately adjusted to match the imposed moments and shape of the distribution. Following the method proposed by Xiu and Karniadakis [25], we approximate the f_{tG} distribution by a pth-order gPC expansion of Jacobi-type polynomials $P_p^{\alpha,\beta}$ of a beta(α, β) distributed random variable. Based on our choice of quadrature, we have found that $\alpha = 8$ and $\beta = 8$ matches the f_{tG} distribution best. For a $p = 7$th-order gPC Jacobi expansion, we have no error in the mean of the distribution and an absolute error in variance of the order of 10^{-7}. The optimal nodes and corresponding weights associated with the beta$(\alpha = 8, \beta = 8)$ distribution are computed with a Gauss–Jacobi quadrature rule. The hybrid gPC polynomial basis is constructed by tensor products of Legendre and Jacobi polynomials, following the same guidelines as the classical approach with a unique polynomial family.

The results are analyzed by means of the variance of M_{is} along the upper surface of the airfoil (Fig. 9). We also consider a fully Gaussian representation of M_∞ for the sake of comparison. In this case, the mean value is kept the same ($\mu_{M_\infty} = 0.65$), and the standard deviation of the parameter is tuned to assign very low probabilities to negative values of M_∞. Figure 9 (left) compares the distribution of variance of M_{is} along the extrados for the three different measures. We note that the injection of truncated Gaussian uncertainty into M_∞ provides results similar to the previous ones, with a somewhat slightly larger variance in most of the region of interest. The obtained curve is less symmetric than the uniform case and bears a similar shape to the fully Gaussian case. The location of the maximum peak remains unchanged for all cases. The inspection of the M_{is} pdf profiles at one specific location along the chord ($x/c = 0.25$) shows that the bipolar trend of the solution probability distribution at this location subsists despite the input Gaussianity (Fig. 9, right). We have checked that the pdf for the truncated Gaussian case has a bounded support, as expected. We note that intermediate values of the response, around $M_{\text{is}} \approx 1.2$, have more chance to appear than in the uniform case. These values will in fact become more dominant, as the standard deviation of the Gaussian-like M_∞ will be reduced.

IV. Conclusions

In this study, a stochastic spectral projection solver based on generalized polynomial chaos expansions was applied to the uncertainty quantification of stochastic compressible flows around a NACA0012 airfoil due to random freestream Mach number and angle of attack. Simple stochastic models were considered in which the freestream Mach number and the angle of attack are represented by independent random variables with bounded supports and uniform and/or truncated Gaussian measures. Since the stochastic solution is directly projected onto each member of the orthogonal basis chosen to span the random space, this method has the advantage of being nonintrusive. Therefore, the stochastic solver was easily coupled with a RSM-RANS deterministic code to extract statistical informations of both the mean flow and the anisotropic turbulent field. The projection step is equivalent to computing multidimensional integrals over the support of the random input probability. In this work, the low stochastic dimensionality of the problem allows numerical quadratures of Gauss type (by full tensor products) to be used to evaluate these integrals.

A careful error analysis of the global representation based on the number of solution samples and the polynomial order at use has allowed a better understanding of the coupling between aliasing error, finite-term projection error, and the numerical error related to the intrinsic numerical approximation of the deterministic solver. Monitoring of pressure and skin-friction coefficients moments along the surface of the airfoil has shown fast convergence rates for global aerodynamic quantities (e.g., lift and drag coefficients) and local quantities such as the isentropic Mach number and the pressure coefficient. Nonetheless, the accuracy of the approximation remains acceptable for derived quantities that are more sensitive to numerical noise, such as the skin friction. It must be noted that for the parametric stochastic ranges of interest, this methodology did not suffer from any lack of robustness, despite strong nonlinearities (due to the shock waves) and a recirculation zone present in the stochastic solution.

As far as the physical aspects are concerned, this study was focussed on the potential importance of dealing with combined angle of attack and freestream Mach number uncertainties. Their consequences on the resulting stochastic flow were demonstrated using a detailed sensitivity analysis conducted with the computation of Sobol's coefficients. This analysis confirmed that the uncertainty present in the freestream Mach number is the driving mechanism in the resulting probability density function of the stochastic aerodynamic field. Nonetheless, once the mean position of the shock wave is constrained by the existence of the separated shear layer, the probability density function of the solution may exhibit a bifurcation corresponding to a jump in the solution, with a most probable value quickly switching from a larger to a lower value.

The impact of nonuniform mixed distributions on the stochastic flow was also investigated. A truncated Gaussian distribution for the freestream Mach number was considered and the results were

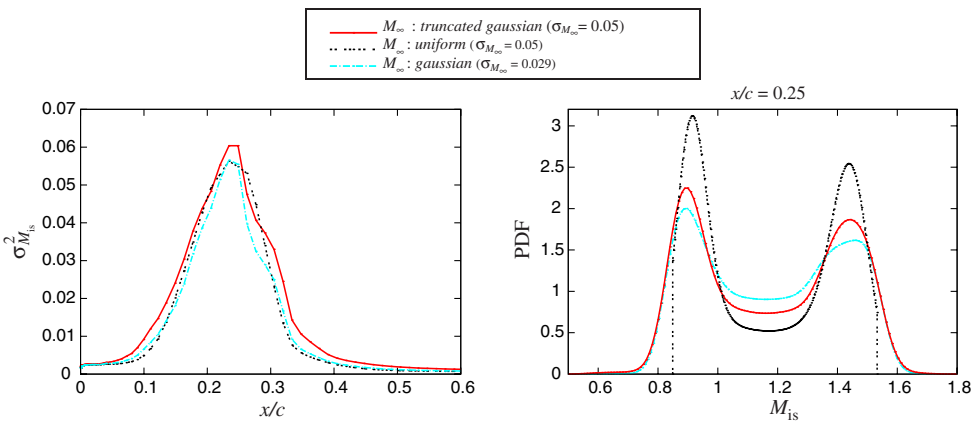

Fig. 9 Comparison of the effect of uniform, Gaussian and truncated Gaussian random distributions of M_∞ with $\mu_{M_\infty} = 0.65$ onto $\sigma^2_{M_{\text{is}}}$ along the upper surface of the airfoil (left) and corresponding pdf computed at $x/c = 0.25$ (right). The angle of attack is modeled using a uniform distribution identical to the one defined in case D.

qualitatively similar to the results obtained for uniform distributions, with a predominance of the freestream Mach number uncertainty onto the solution variability.

The results presented in this study aim to demonstrate the relevant capabilities of the pseudospectral stochastic representation for uncertainty quantifications with viscous steady shocked flows. Because of its high accuracy in the representation of the solution statistics at relatively low computational cost, this approach combined with the development of efficient adaptive sparse quadrature procedures represents a promising tool for the development of robust shape design methodologies.

Appendix A: Preliminary Error Analysis

The global error of the stochastic projection gPC representation can be seen as a superposition of an aliasing error (coming from the interpolation related to the numerical quadrature), a finite-term projection error (due to the truncated gPC representation), and a numerical error due to the intrinsic numerical approximation of the deterministic solver. In this context, classical assessment of numerical accuracy of the method through convergence analysis becomes intricate. When studying stochastic approximations, it is common sense to wish the numerical errors associated with the deterministic solver to be independent and of smaller magnitude than the other errors. In the following, we will try to show with an example followed by some explanations that it is better to handle sources of errors of comparable magnitude. Then we will carry out a complete convergence study for the four stochastic flow regimes investigated in the paper.

Here, we conduct a preliminary study on the accuracy of the present gPC formulation on a simplified model that is drawn from the configuration of case D by considering the angle of attack as deterministic ($\alpha = 5$ deg). The freestream Mach number is modeled as a uniform random variable characterized by $\mu_{M_\infty} = 0.65$ and $\sigma_{M_\infty} = 0.05$. This simple one-random-parameter study is relevant, as it is more stringent on the numerical representation than a two-random-parameter study. Indeed, we will see that uncertainty in the angle of attack introduces additional smoothing to the solution statistics, due to data scattering.

Stochastic results computed using Gauss–Legendre (GL) quadrature with $n_q = 8$ points are compared with those obtained with a Gauss–Kronrod (GK) quadrature rule [31]. The GK rule only requires the computation of $n_q + 1$ additional points, compared with the GL grid, i.e., nine new runs in the present case.

Figure A1 presents a comparison between these two approaches on the computation of the mean of $\mu_{M_{is}}$ and μ_{C_f} over the airfoil extrados. The accuracy of the mean solution only depends on the aliasing error via n_q and the spatial discretization error. In addition, the figures display the different realizations (corresponding to the GL and GK points) as well as the spatial grid. When the mean solution is

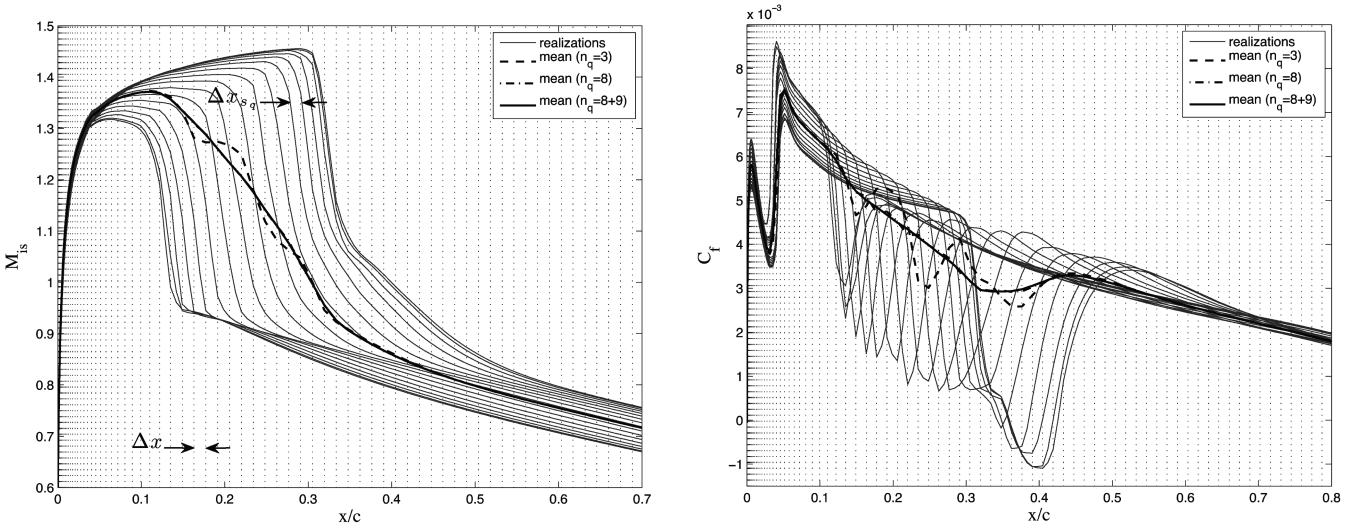

Fig. A1 Effect of aliasing error: realizations and corresponding mean profiles of $\mu_{M_{is}}$ (left) and C_f (right) for different quadrature levels (Gauss–Legendre vs Gauss–Kronrod) (case D*, $\alpha = 5$ deg, $\mu_{M_\infty} = 0.65$, and $\sigma_{M_\infty} = 0.05$). Note that case D* is similar to case D but with deterministic angle of attack.

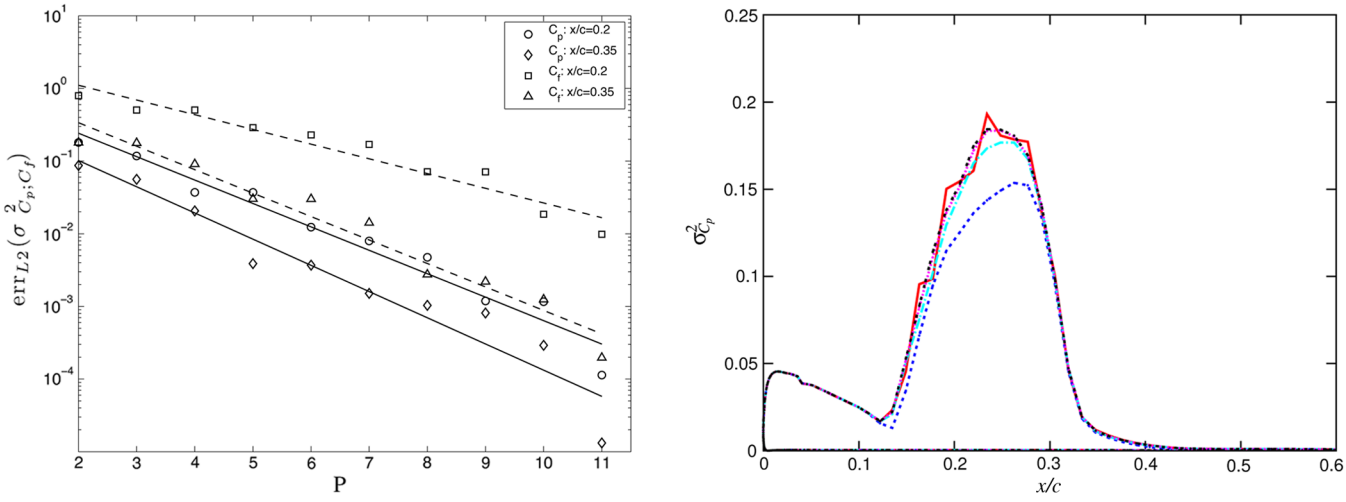

Fig. A2 Effect of truncation error: C_p variance distribution along the extrados for different choices of gPC truncation (right) and convergence rates of the solution variance (left) vs the polynomial order P (case D*, $\alpha = 5$ deg; $\mu_{M_\infty} = 0.65$, and $\sigma_{M_\infty} = 0.05$).

computed from the eight GL points or the $(8+9)$ GK points, the profiles are very similar and smooth. However, when one only uses $n_q = 3$ points, the results are disastrous, with strong oscillations (stairlike profile) due to aliasing.

Next, we investigate the coupling between aliasing and truncation errors by considering higher moments. Figure A2 presents results for $\sigma^2_{C_p}$ and $\sigma^2_{C_f}$. In this case, the accuracy of the solution variance depends on the aliasing error via n_q, the truncation error via P, and the spatial discretization error. Assuming that the latter is of comparable magnitude with the other two, we investigate the effect of n_q and P.

Figure A2 (right) shows the distribution of $\sigma^2_{C_p}$ for different combinations of quadratures and truncations. When the integration is sufficiently resolved, as in the case of the GK quadrature with 17 points, the results are very smooth and $P = 7$th- or 12th-order approximations (maximum polynomial exactness we can afford) provide very similar profiles for the variance. Although it is clearly visible that the increase of the quadrature accuracy (GL $\rightarrow$ GK) notably improves the solution locally by suppressing the spurious oscillations observed on the results of the seventh-order gPC expansion (i.e., $n_q = 8$), we conclude that the sensitivity of the stochastic aerodynamic coefficients can reasonably be captured using a relative smaller number of quadrature points.

Figure A2 (left) displays the relative error in variance based on the best estimate (obtained for $P = 12$), as no other reference solution is available (Monte Carlo solutions would be too costly for this level of accuracy). Open symbols represent our computations, and the decay rates are linearly fitted in a semilogarithmic scale (solid lines are $\sigma^2_{C_p}$ and dashed lines are $\sigma^2_{C_f}$). We note that we get close to spectral convergence up to high order for both coefficients. The convergence rate is similar for both quantities at the different locations, except for the skin friction at $x/c = 0.2$, for which the solution converges somewhat slower.

In conclusion, the level of accuracy of our stochastic representation depends on the type of statistics and the choice of the physical quantity under consideration as well as the spatial location at which this quantity is monitored. Moreover, it seems that there exists a coupling between deterministic and stochastic errors that interplays through the two levels of discretization.

Appendix B: Spatial and Stochastic Grid Requirements

Some results from the literature suggest that global gPC approximation based on spectral projection is not appropriate in the case of discontinuous or sharp solutions. In this case, the continuous approximated solution may exhibit some oscillations, inducing irregular and unphysical patterns in the spatial distribution of the solution moments or pdf, e.g., stairlike profile for the mean solution [7]. The location of these irregularities coincides with the collocation points and is more notable for local physical quantity (such as Cf), which is more sensitive to discretization errors.

Given a fixed spatial discretization grid of typical resolution size Δx along the chord, the accuracy of the gPC approximation depends on the choice of P and n_q. Let us call $p_{s_q} \equiv p(x_{s_q}, Z_q)$ the value of the discontinuous solution at the location of the shock x_{s_q} obtained for the quadrature point Z_q [cf. Fig. A1 (left)]. When the number n_q of collocation points is not sufficient, it may happen that $\Delta x_{s_q} \gg \Delta x$ and the problem described hereinbefore appears [12]. However, several of our studies have shown that the profiles recover regularity when we increase n_q as $\Delta x_{s_q} \rightarrow \Delta x$. This is the case in Fig. A1 for sufficiently high n_q. In the case in which $\Delta x_{s_q} \ll \Delta x$, one faces aliasing error, as the shocks are not assigned to the correct cell in physical space. For some higher moments or pdf contours, some oscillations may remain along the distribution (cf. Fig. A2 (right) for $n_q = 8$ and $P = 7$), but the right profile magnitude is generally captured for a good (n_q, P) choice.

It is generally difficult to predict the appropriate n_q, as the average Δx_{s_q} is not known a priori. The latter depends on the distribution of the chosen quadrature rule as well as the sensitivity of the response to the parametric uncertainty. This sensitivity relates to the span length of the geometric envelop in which all probable discontinuous events may take place. Nonlinearity of the model, monotonicity of the response, and airfoil geometry will affect differently this range.

In conclusion, there exists a strong coupling between the discretization in physical space and the stochastic grid in random space. As a result, refinement of the grid in one of the two spaces *must* happen together within the other one.

Appendix C: Convergence Analysis of the Stochastic Transonic Flow Representation

This Appendix presents a detailed convergence study for the four stochastic transonic flow regimes based on uniform random distributions of the uncertain angle of attack and freestream Mach number (cf. Sec. III.B). Based on our previous analysis and considering our level of confidence in the accuracy of the spatial discretization provided by the choice of our computational grid [37], we design a stochastic grid that matches (in most situations) the requirement described in the previous section. This choice also reflects the computational bottleneck induced by the numerical cost related to the uncertainty propagation. In this study, the number of quadrature points is fixed to $n_q = 8$ along each direction and is an appropriate tradeoff between accuracy and computational burden.

First, the convergence properties of the global aerodynamic coefficient are presented. The relative errors of the lift-and-drag variances versus various polynomial order P are reported in Table C1 for each stochastic flow regime investigated in Sec. III.B. Because we do not have an exact reference solution to compare with, the error is monitored as the normalized L_2 norm of the difference of a given flow quantity between the stochastic solution of interest and that of the most resolved computation (obtained using $P = 7$) that we pick as our reference solution. Typically, we have seen that an increase from $P = 2$ to 6 permits a substantial reduction of the truncation error of the gPC expansion.

Next, the effect of the polynomial order P on the accuracy of the gPC formulation was investigated for the most difficult case, i.e., case D. Figure C1 shows the influence of the number of quadrature points n_q on the mean solution of the isentropic Mach number.

Although a relatively small number of quadrature points $(2 \leq n_q \leq 4)$ is sufficient to capture correctly the zero-order moment of the solution, it is not sufficient for the $0.1 < x/c < 0.3$ region (Fig. C1, right). As explained previously, this is due to the fact that this region is strongly affected by the aerodynamic nonlinearities related to shock waves and that the stochastic quadrature grid is not refined enough compared with the spatial resolution. It is then

Table C1 Relative error of the lift-and-drag variance versus the polynomial order P for the four stochastic flow regimes[a]

	$\mathrm{err}_{L2}(\sigma^2_L)$				$\mathrm{err}_{L2}(\sigma^2_D)$			
P	A	B	C	D	A	B	C	D
2	2.021E − 5	2.383E − 4	3.156E − 3	5.168E − 3	1.981E − 4	3.796E − 2	1.537E − 4	8.554E − 4
3	7.776E − 7	1.963E − 5	2.249E − 5	5.058E − 4	2.977E − 5	1.040E − 3	9.318E − 4	2.267E − 4
4	5.016E − 7	1.690E − 5	1.248E − 5	7.946E − 5	1.940E − 5	4.663E − 4	1.978E − 4	5.013E − 6
5	3.455E − 7	1.358E − 5	1.987E − 6	4.551E − 5	1.588E − 5	5.966E − 5	3.973E − 5	3.289E − 6
6	1.995E − 7	5.042E − 6	1.235E − 6	2.592E − 5	1.137E − 5	8.405E − 6	2.434E − 5	1.112E − 6

[a]For case A, $\alpha = 3$ deg and $M_\infty = 0.55$; for case B, $\alpha = 3$ deg and $M_\infty = 0.65$; for case C, $\alpha = 5$ deg and $M_\infty = 0.55$; and for case D, $\alpha = 5$ deg and $M_\infty = 0.65$.

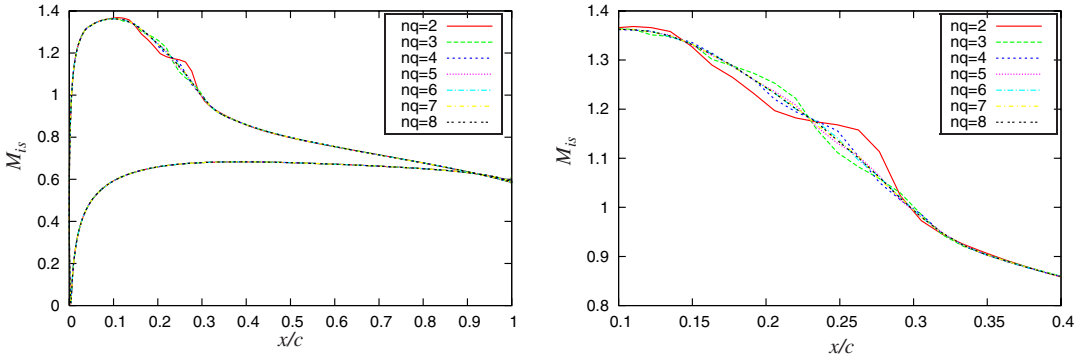

Fig. C1 Effect of the number of collocation points n_q on the distribution of the mean value of M_{is} for case D, $\mu_\alpha = 5$ deg and $\mu_{M_\infty} = 0.65$.

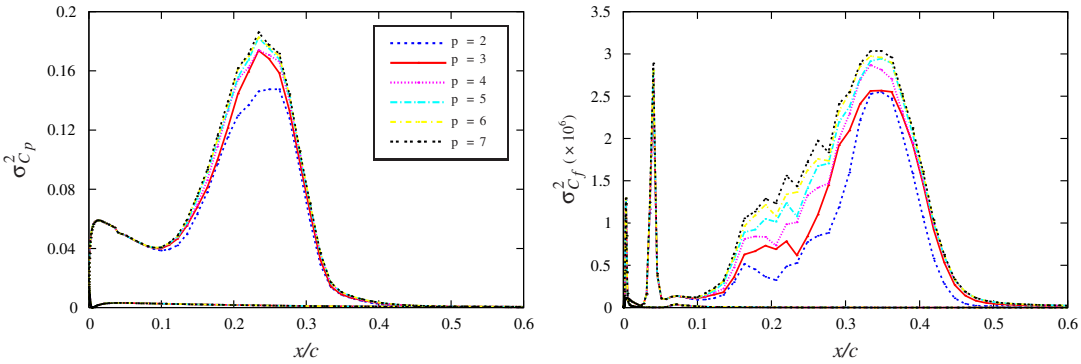

Fig. C2 Influence of the polynomial order P on the pressure coefficient C_p and the skin-friction C_f variances along the airfoil surfaces (case D).

necessary to increase the number of collocation points per random dimension up to $n_q = 6$ to obtain converged and smooth values of the mean distribution of M_{is}.

Next, the convergence analysis of the variance distribution of the pressure coefficient C_p and the skin-friction coefficient C_f along the upper surface of the airfoil is presented. Figure C2 (left), which shows the distribution of $\sigma^2_{C_p}$, reveals that the peak of flow variability at $x/c = 0.28$ is adequately captured for $P \geq 5$.

However, we can clearly see in Fig. C2 (right) that a fully converged representation of the $\sigma^2_{C_f}$ distribution is more problematic to achieve. It is then necessary to increase the polynomial order up to $P = 7$ to get an almost-converged prediction of the variance of the skin-friction coefficients. Note that, similar to the case discussed in Fig. A2 (right), the use of a seventh-order gPC expansion does not fully remove all nonphysical oscillations for $0.15 \leq x/c \leq 0.3$ (Fig. C2, right). Indeed, the skin friction is a very sensitive quantity to numerical noise.

Figure C3 shows the convergence error of $\sigma^2_{C_p}$ and $\sigma^2_{C_f}$ for $x/c = 0.2$, 0.35, and 0.7. Open symbols represent the computations and the decay rates are linearly fitted in a semilogarithmic scale (solid lines are $\sigma^2_{C_p}$ and dashed lines are $\sigma^2_{C_f}$). It is confirmed that the convergence rates obtained for $\sigma^2_{C_p}$ are better than those computed for $\sigma^2_{C_f}$. Moreover, we observe that the sensitivity level of the stochastic flowfield (as shown, for instance, at $x/c = 0.2$ in Fig. C2, right) results in some deterioration of the convergence rate. Convergence rates are best when the solution is regular (e.g., $x/c = 0.7$).

With this error analysis, we have shown that our choice of physical and stochastic discretization level, although being in part subject to numerical cost constraints, provides a very accurate approximation of global aerodynamic quantities (e.g., lift and drag coefficients) and local quantities such as the isentropic Mach number and the pressure coefficient. It has been observed that the accuracy of our approximation remains acceptable for derived quantities, which are more sensitive to numerical noise, such as the skin friction.

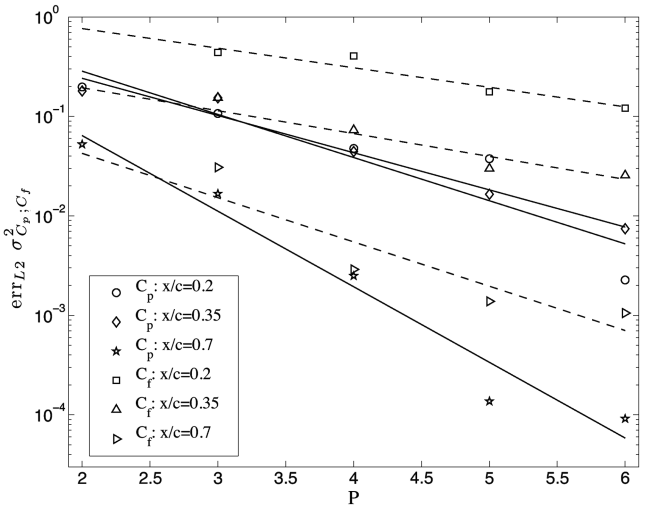

Fig. C3 Convergence rate of the pressure coefficient C_p and the skin-friction C_f variances with respect to P (case D).

Acknowledgments

A preliminary version of this work was presented at the 5th ECCOMAS conference, 30 June–4 July 2008. Parallel Computing Resources (AMD Opteron Dual Core Model 265 1.8 GHz) were made available at the Institut Jean Le Rond d'Alembert (Université Pierre et Marie Curie).

References

[1] Pettit, C., "Uncertainty Quantification in Aeroelsticity: Recent Results and Research Challenges," *Journal of Aircraft*, Vol. 41, No. 5, 2004, pp. 1217–1229.
doi:10.2514/1.3961

[2] Beran, P., Pettit, C., and Millman, D., "Uncertainty Quantification of Limit-Cycle Oscillations," *Journal of Computational Physics*, Vol. 217, No. 1, 2006, pp. 217–247.
doi:10.1016/j.jcp.2006.03.038

[3] Witteveen, J., and Bijl, H., "An Unsteady Adaptative Stochastic Finite Elements Formulation for Rigid-Body Fluid-Structure Interaction," *Computers and Structures*, Vol. 86, Nos. 23–24, 2008, pp. 2123–2140. doi:10.1016/j.compstruc.2008.06.009

[4] Witteveen, J., Loeven, A., Sarkar, S., and Bijl, H., "Probabilistic Collocation for Period-1 Limit Cycle Oscillations," *Journal of Sound and Vibration*, Vol. 311, Nos. 1–2, 2008, pp. 421–439. doi:10.1016/j.jsv.2007.09.017

[5] Le Meitour, J., Lucor, D., and Chassaing, J.-C., "Stochastic Aeroelastic Analysis of a Pitching and Plunging Airfoil in an Incompressible Flow," International Forum on Aeroelasticity and Structural Dynamics, Seattle, WA, Paper 2009-027, June 2009.

[6] Millman, D., King, P., and Beran, P., "Airfoil Pitch-and-Plunge Bifurcation Behavior with Fourier Chaos Expansions," *Journal of Aircraft*, Vol. 42, No. 2, 2005, pp. 376–384. doi:10.2514/1.5550

[7] Loeven, G., Witteven, J., and Bijl, H., "Probabilistic Collocation: An Efficient Nonintrusive Approach for Arbitrarily Distributed Parametric Uncertainties," AIAA Paper 2007-317, 2007.

[8] Witteveen, J., Sarkar, S., and Bijl, H., "Modeling Physical Uncertainties in Dynamic Stall Induced Fluid-Structure Interaction of Turbine Blades Using Arbitrary Polynomial Chaos," *Computers and Structures*, Vol. 85, Nos. 11–14, 2007, pp. 866–878. doi:10.1016/j.compstruc.2007.01.004

[9] Asokan, B. V., and Zabaras, N., "Variational Multiscale Stabilized FEM Formulations for Transport Equations: Stochastic Advection-Diffusion and Incompressible Stochastic Navier–Stokes Equations," *Journal of Computational Physics*, Vol. 202, No. 1, 2005, pp. 94–133. doi:10.1016/j.jcp.2004.06.019

[10] Lucor, D., Meyers, J., and Sagaut, P., "Sensitivity Analysis of LES to Subgrid-Scale-Model Parametric Uncertainty Using Polynomial Chaos," *Journal of Fluid Mechanics*, Vol. 585, 2007, pp. 255–279. doi:10.1017/S0022112007006751

[11] Ko, J., Lucor, D., and Sagaut, P., "Sensitivity of Two-Dimensional Spatially Developing Mixing Layers with Respect to Uncertain Inflow Conditions," *Physics of Fluids*, Vol. 20, No. 7, 2008, pp. 077102–077120. doi:10.1063/1.2937465

[12] Poëtte, G., Després, B., and Lucor, D., "Uncertainty Quantification for Systems of Conservation Laws," *Journal of Computational Physics*, Vol. 228, No. 7, 2009, pp. 2443–2467. doi:10.1016/j.jcp.2008.12.018

[13] Mathelin, L., Hussaini, M., and Zang, T., "Stochastic Approaches to Uncertainty Quantification in CFD Simulations," *Numerical Algorithms*, Vol. 38, No. ', 2005, pp. 209–236.

[14] Lin, G., Su, S.-H., and Karniadakis, G., "Predicting Shock Dynamics in the Presence of Uncertainties," *Journal of Computational Physics*, Vol. 217, No. 1, 2006, pp. 260–276. doi:10.1016/j.jcp.2006.02.009

[15] Hosder, S., Walters, R., and Perez, R., "A Nonintrusive Polynomial Chaos Method for Uncertainty Propagation in CFD Simulations," AIAA Paper 2006-891, 2006.

[16] Hosder, S., Walters, R., and Balch, M., "Efficient Sampling for Non-Intrusive Polynomial Chaos Applications with Multiple Uncertain Input Variables," AIAA Paper 2007-1939, 2007.

[17] Xiu, D., and Hesthaven, J. S., "High-Order Collocation Methods for Differential Equations with Random Inputs," *Journal of Scientific Computing*, Vol. 27, No. 3, 2005, pp. 1118–1139. doi:10.1137/040615201

[18] Tatang, M., Pan, W., Prinn, R., and McRae, G., "An Efficient Method for Parametric Uncertainty Analysis of Numerical Geophysical Models." *Journal of Geophysical Research*, Vol. 102, 1997, pp. 21925–21932. doi:10.1029/97JD01654

[19] Babuška, I., Nobile, F., and Tempone, R., "A Stochastic Collocation Method for Elliptic Partial Differential Equations with Random Input Data," *SIAM Journal on Numerical Analysis*, Vol. 45, No. 3, 2007, pp. 1005–1034. doi:10.1137/050645142

[20] Xiu, D., and Karniadakis, G., "The Wiener-Askey Polynomial Chaos for Stochastic Differential Equations," *SIAM Journal on Scientific Computing*, Vol. 24, No. 2, 2002, pp. 619–644. doi:10.1137/S1064827501387826

[21] Wiener, N., "The Homogeneous Chaos," *American Journal of Mathematics*, Vol. 60, 1938, pp. 897–936. doi:10.2307/2371268

[22] Ghanem, R., and Spanos, P., *Stochastic Finite Elements: A Spectral Approach*, Springer–Verlag, New York, 1991.

[23] Sobol', I. M., "Sensitivity Analysis for Nonlinear Mathematical Models*Mathematical Modelling & Computational Experiment*, Vol. 1, 1993, pp. 407–414.

[24] Wand, M., and Jones, M., *Kernel Smoothing*, Monographs on Statistics and Applied Probability 60, Chapman and Hall/CRC, Boca Raton, FL, 1995.

[25] Xiu, D., and Karniadakis, G., "Supersensitivity Due to Uncertain Boundary Conditions," *International Journal for Numerical Methods in Engineering*, Vol. 61, No. 12, 2009, pp. 2114–2138.

[26] Keese, A., "Numerical Solution of Systems with Stochastic Uncertainties: A General Purpose Framework for Stochastic Finite Elements," Ph.D. Thesis, Technische Universität Braunschweig, Mechanik-Zentrum, Braunschweig, Germany, 2005.

[27] Novak, E., and Ritter, K., "Simple Cubature Formulas with High Polynomial Exactness," *Constructive Approximation*, Vol. 15, No. 4, 1999, pp. 499–522. doi:10.1007/s003659900119

[28] Smolyak, S., "Quadrature and Interpolation Formulas for Tensor Products of Certain Classes of Functions," *Soviet Mathematics, Doklady*, Vol. 4, 1963, pp. 240–243.

[29] Kronrod, A. S., "Nodes and Weights of Quadrature Formulas," Consultants Bureau, MR 32:598, New York, 1965 (English translation).

[30] Patterson, T., "The Optimum Addition of Points to Quadrature Formulae," *Mathematics of Computation*, Vol. 22, No. 104, 1968, pp. 847–856. doi:10.2307/2004583

[31] Laurie, D., "Calculation of Gauss–Kronrod Quadrature Rules," *Mathematics of Computation*, Vol. 66, No. 219, 1997, pp. 1133–1145. doi:10.1090/S0025-5718-97-00861-2

[32] Gautschi, W., *Orthogonal Polynomials: Computation and Approximation*, Numerical Mathematics and Scientific Computation, Oxford Univ. Press, Oxford, 2004.

[33] Petras, K., "On the Smolyak Cubature Error for Analytic Functions," *Advances in Computational Mathematics*, Vol. 12, No. 1, 2000, pp. 7193.

[34] Gerolymos, G., and Vallet, I., "Wall-Normal-Free Near-Wall Reynolds-Stress Closure for 3-D Compressible Separated Flows," *AIAA Journal*, Vol. 39, No. 10, 2001, pp. 1833–1842. doi:10.2514/2.1179

[35] Gerolymos, G., Sauret, E., and Vallet, I., "Contribution to the Single-Point-Closure Reynolds-Stress Modelling of Inhomogeneous Flow," *Theoretical and Computational Fluid Dynamics*, Vol. 17, Nos. 5–6, 2004, pp. 407–431. doi:10.1007/s00162-004-0109-5

[36] Chassaing, J.-C., Gerolymos, G., and Vallet, I., "Efficient and Robust Computation of 3-D Compressible Flows with Reynolds-Stress Closure," *AIAA Journal*, Vol. 41, No. 5, 2003, pp. 763–773. doi:10.2514/2.2030

[37] Chassaing, J.-C., Gerolymos, G., and Vallet, I., "Reynolds-Stress Model Dual-Time-Stepping Computation of Unsteady 3-D Flows," *AIAA Journal*, Vol. 41, No. 10, 2003, pp. 1882–1894. doi:10.2514/2.1904

[38] Jaynes, E., "Information Theory and Statistical Mechanics," *Physical Review*, Vol. 106, No. 4, 1957, pp. 620–630. doi:10.1103/PhysRev.106.620

[39] Newman, J., Newman, P., Taylor, A., and Hou, G.-W., "Efficient Nonlinear Static AeroelasticWing Analysis," *Computers and Fluids*, Vol. 28, Nos. 4–5, 1999, pp. 615–628. doi:10.1016/S0045-7930(98)00047-4

[40] Palacios, R., and Cesnik, C., "Static Nonlinear Aeroelasticity of Flexible Slender Wings in Compressible Flow," AIAA Paper 2005-1945, 2005.

[41] Duvigneau, R., "Robust Design of a Transonic Wing with Uncertain Mach Number," *EUROGEN 2007 Evolutionary Methods for Design, Optimization and Control*, Jyväskylä, Finland, 11–13 June 2007.

[42] Parussini, L., Pediroda, V., and Obayashi, S., "Design Under Uncertainties of Wings in Transonic Field," *JSME International Journal, Series B (Fluids and Thermal Engineering)*, Vol. 48, No. 2, 2005, pp. 218–223. doi:10.1299/jsmeb.48.218

[43] Bartels, R., "Flow and Turbulence Modeling and Computation of Shock Buffet Onset for Conventional And Supercritical Airfoils," NASA TP-1998-206908, 1998.

[44] Ko, J., "Application des Polynômes de Chaos à la Simulation d'Ecoulements Convectifs Incertains," Ph.D. Thesis, Univ. Pierre et Marie Curie, Paris, 2009.

P. Beran
Associate Editor